Time-of-Flight Information Improved the Detectability of Subcentimeter Spheres Using a Clinical PET/CT Scanner

Naoki Hashimoto[1], Keishin Morita[1], Yuji Tsutsui[1,2], Kazuhiko Himuro[2], Shingo Baba[2], and Masayuki Sasaki[1]

[1]Department of Health Sciences, Graduate School of Medical Sciences, Kyushu University, Fukuoka, Japan; and [2]Division of Radiology, Department of Medical Technology, Kyushu University, Fukuoka, Japan

Recent advancements in clinical PET/CT scanners have improved the detectability of small lesions. However, the ideal reconstruction parameters for detecting small lesions have not yet been sufficiently clarified. The purpose of this study was to investigate the detectability of subcentimeter spheres using a clinical PET/CT scanner. **Methods:** We used a clinical PET/CT scanner to obtain the data of a National Electrical Manufacturers Association body phantom consisting of 6 small spheres (inner diameters, 4.0, 5.0, 6.2, 7.9, 10, and 37 mm) containing ^{18}F solution. The background activity was 2.65 kBq/mL, and the sphere-to-background ratio was 8. The PET data obtained for 2 and 120 min were reconstructed using ordered-subsets expectation maximization (OSEM), OSEM + point-spread function (PSF), and OSEM + time-of-flight (TOF) with voxel sizes of 2.04 × 2.04 × 2.00 mm (2-mm voxels) and 4.07 × 4.07 × 3.99 mm (4-mm voxels). A gaussian filter was not used. The image quality was evaluated by visual assessment, as well as by physical assessment of the detectability index and recovery coefficients. **Results:** According to the visual assessment, the detectability of the spheres improved using TOF and a longer acquisition. Using the OSEM+TOF model, the smallest visually detected spheres were 5 mm in diameter with a 120-min acquisition and 6 mm in diameter with a 2-min acquisition. According to physical assessment, the detectability of spheres 10 mm or smaller using the OSEM+TOF image was superior to that using the OSEM image. In addition, the detectability of each hot sphere and recovery coefficient with 2-mm voxels was superior to that with 4-mm voxels. Although OSEM+PSF images showed less background noise, detectability and the recovery coefficient were not improved for spheres 8 mm or smaller. **Conclusion:** The TOF model with 2-mm voxels improved the detectability of subcentimeter hot spheres on a clinical PET/CT scanner.

Key Words: instrumentation; PET/CT; point-spread function; small voxel size; subcentimeter sphere; time-of-flight

J Nucl Med Technol 2018; 46:268–273
DOI: 10.2967/jnmt.117.204735

PET/CT using ^{18}F-FDG is a useful tool for making a diagnosis, staging disease, evaluating the response to therapy, and performing prognostic stratification (*1–3*). Limitations associated with the PET/CT images include false-negative results and underestimation of small accumulations because of the partial-volume effect. The partial-volume effect is caused by both the finite resolution effect and the tissue fraction effect (*4*). Because the partial-volume effect strongly depends on the size of the tumor, the smaller the tumor, the greater the underestimation of the uptake (*5*). Because the detection limit is assumed to be approximately 1 cm in conventional PET/CT, the PET/CT image quality is usually evaluated using a 10-mm hot-sphere phantom (*6*). Our previous study also determined the reconstruction parameters for detecting 10-mm hot spheres on PET/CT images (*7*).

Recent advancements in the hardware and software of PET/CT devices have improved the detectability of small lesions. Lutetium orthosilicate and lutetium yttrium orthosilicate, which have a high light output and excellent timing resolution, have made the time-of-flight (TOF) information practical in the reconstruction algorithm (*8*). The TOF technique measures the difference in time between the detection of 2 photons in coincidence and allows for more precise estimation of the annihilation location along the line of response. TOF also improves the signal-to-noise ratio of PET images (*9*). Point-spread function (PSF) correction incorporates accurately measured PSFs into the reconstruction algorithm, thereby reducing blurring and distortion of the final image (*10*). PSF modeling is expected to improve both the signal-to-noise ratio and the spatial resolution of PET images (*11–13*). Both TOF and PSF have been reported to improve the quality and lesion detectability of PET images (*14–16*).

Recently, an increasing number of studies have examined small lesions, such as arteriosclerosis and lymph node metastases smaller than 10 mm in diameter (*17,18*). However, the ideal reconstruction parameters for the detection of such small lesions have not yet been sufficiently clarified. The purpose of this study was to investigate the ideal reconstruction setting for the detection of subcentimeter hot lesions using a clinical PET/CT scanner.

Received Nov. 6, 2017; revision accepted Jan. 6, 2018.
For correspondence or reprints contact: Masayuki Sasaki, Department of Health Sciences, Graduate School of Medical Sciences, Kyushu University, 3-1-1 Maidashi, Higashi-ku, Fukuoka 812-8582, Japan.
E-mail: msasaki@hs.med.kyushu-u.ac.jp
Published online Mar. 29, 2018.

MATERIALS AND METHODS

Phantoms

We used a National Electrical Manufacturers Association International Electrotechnical Commission body phantom (NEMA phantom) consisting of 6 spheres with inner diameters of 37, 10, 7.9, 6.2, 5.0, and 4.0 mm (Micro Hollow Sphere Sets (*4*); Data Spectrum Corp.) (Fig. 1). The background compartment and the 6 spheres were filled with ^{18}F solution such that there was a sphere-to-background ratio of 8. The background radioactivity of the ^{18}F solution was 2.65 kBq/mL, in accord with Japanese guidelines for oncologic ^{18}F-FDG PET/CT data acquisitions (*6*). The standard background radioactivity in Japanese subjects, 60 kg, is estimated to be 2.65 kBq/mL at 60 min after injection of 3.7 MBq of ^{18}F-FDG per kilogram.

Data Acquisition and Image Reconstruction

We used a Biograph mCT scanner (Siemens Healthcare) for all PET acquisitions in this study. This brand of scanner comprises 3 rings with a total of 144 lutetium orthosilicate $4.0 \times 4.0 \times 20$ mm crystals covering an axial field of view of 16.2 cm and a transaxial field of view of 70 cm. The coincidence time window was 4.1 ns. The TOF time resolution was 555 ps. The spatial resolution at 1 and 10 cm from the center of the field of view was 4.4 and 4.9 mm in full width at half maximum, respectively. The PET data were acquired in 3-dimensional list mode for 120 min. Three 2-min PET acquisitions and one 120-min PET acquisition were reconstructed and evaluated for the detectability of each sphere. The images were reconstructed using baseline ordered-subsets expectation maximization (OSEM), OSEM+PSF, and OSEM+TOF. The reconstruction parameters were determined by evaluating image quality, contrast of hot spheres, and background variability according to our previous study (*5*). The parameters for OSEM and OSEM+PSF were 3 iterations and 24 subsets, whereas those for OSEM+TOF were 2 iterations and 21 subsets. The available subset number for the TOF model was restricted to 21, whereas that nearest 21 for OSEM+PSF in our PET/CT scanner was 24. A gaussian filter was not applied. The voxel size of the reconstructed images was $2.04 \times 2.04 \times 2.00$ mm (2-mm voxels) and $4.07 \times 4.07 \times 3.99$ mm (4-mm voxels). CT data for attenuation correction were obtained by a whole-body CT scan obtained using 120 kV, 100 mA, a 0.5-s tube rotation, and a 5-mm slice collimation.

Image Analyses

For the visual assessment, the PET images were evaluated for sphere detectability using a 5-score scale (1, definitely absent; 2, probably absent; 3, equivocal; 4, probably present; and 5, definitely present) by a board-certified nuclear medicine physician and 3 radiologic technologists. They evaluated the images in random order and were masked to the reconstruction parameters. The scores of the 4 observers were averaged. A mean score larger than 3 was considered to indicate that the sphere was present. Spheres with a score of 1 were excluded from the physical assessment.

For the physical assessment of image quality, a circular region of interest (ROI) was placed on each hot sphere with guidance from the CT images, using PMOD software (version 3.607; PMOD Technologies Ltd.). We also placed 12 circular 10-mm-diameter ROIs on the slice at the center of the sphere and on slices ± 1 and ± 2 cm away from the central slice (total of 60 ROIs on 5 slices) in each set of PET images. The coefficient of variance for the background (CV), the detectability of each hot sphere (detectability index [DI]), and the recovery coefficient (RC) were calculated according to the following respective equations:

$$CV = SD_{BG}/Ct_{BG,mean} \times 100$$

$$DI = \left(Ct_{Hot,max} - Ct_{BG,mean}\right)/SD_{BG}$$

$$RC = Ct_{Hot,max}/Ct_{37mmHot,max},$$

where $Ct_{Hot,max}$ is the maximum count for each hot-sphere ROI, $Ct_{BG,mean}$ is the mean of the mean count in 60 background ROIs, SD_{BG} is the SD of the 60 background ROIs, and $Ct_{37mmHot,max}$ is the maximum count for the 37-mm hot-sphere ROI.

Statistical Analysis

Differences in visual score, CV, DI, and RC among OSEM, OSEM+PSF, and OSEM+TOF were analyzed with paired *t* tests, with a *P* value of less than 0.05 considered statistically significant. Interobserver agreement for visual score was evaluated by κ-statistics (poor agreement, $\kappa = 0$; slight agreement, $\kappa = 0.01$–0.20; fair agreement, $\kappa = 0.21$–0.40; moderate agreement, $\kappa = 0.41$–0.60; good agreement, $\kappa = 0.61$–0.80; excellent agreement, $\kappa = 0.81$–1.0).

RESULTS

The 120-min PET acquisitions reconstructed with the various algorithms are shown in Figure 2A. On OSEM+TOF images, the small hot spheres were better seen and the background noise lower than on OSEM images. In terms of background uniformity, OSEM+PSF images were superior to OSEM images. These patterns were also observed for the 2-min acquisitions (Fig. 2B). Regarding differences in voxel size on the 120-min acquisitions, all spheres were more clearly observed with 2-mm voxels than with 4-mm, especially the 5-mm spheres. However, the 2-min acquisitions showed increased background noise, and the hot spheres were relatively unclear.

Figure 3 shows the visual assessment of PET images in relation to the reconstruction algorithms with 4- and 2-mm voxels. For the 120-min acquisitions (Figs. 3A and 3B), visual scores for OSEM+TOF images were higher than those for OSEM images. The visual score for 5-mm or larger spheres with 4-mm voxels exceeded the criterion of 3. On OSEM+TOF images with 4-mm voxels, the visual

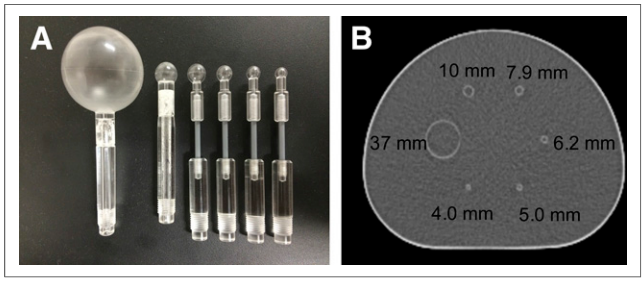

FIGURE 1. (A) Photograph of hot sphere phantoms. (B) Axial CT image of NEMA phantom with spheres.

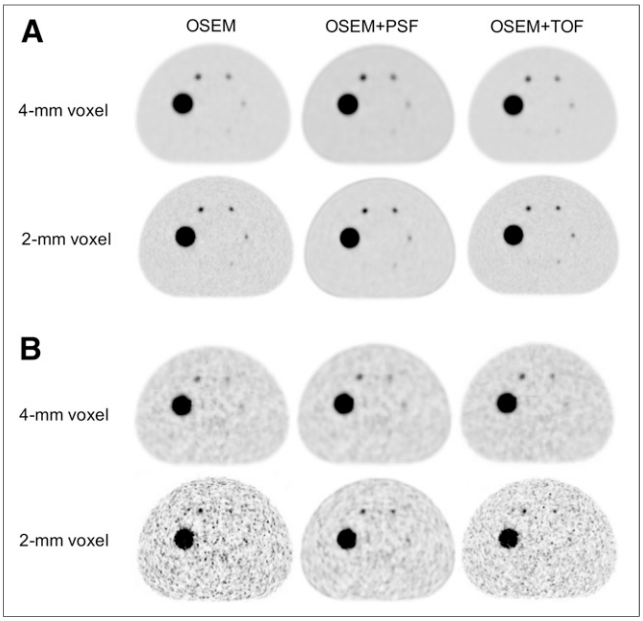

FIGURE 2. Use of different reconstruction algorithms on PET images of phantom. (A) On 120-min acquisition, small hot spheres were better seen on TOF images and on images reconstructed with 2-mm voxels. (B) On 2-min acquisition, a similar pattern was observed.

scores for 6-, 5-, and 4-mm spheres were 4.5 ± 0.58, 3.3 ± 0.50, and 1.3 ± 0.50, respectively, whereas those with 2-mm voxels were 5.0 ± 0.00, 4.0 ± 0.00, and 2.5 ± 0.58, respectively. On OSEM images with 4-mm voxels, the visual scores for 6-, 5-, and 4-mm spheres were 4.3 ± 0.50, 3.0 ± 0.00, and 1.3 ± 0.50, respectively, whereas those with 2-mm voxels were 4.8 ± 0.50, 3.5 ± 1.00, and 1.5 ± 0.58, respectively. The visual scores for 5- and 6-mm spheres with 2-mm voxels were higher than those with 4-mm voxels (Figs. 3A and 3B). In the 2-min acquisitions (Figs. 3C and 3D), the visual scores for OSEM+TOF images were higher than those for OSEM images, whereas those for OSEM+PSF images were the highest. For OSEM+TOF images with 4-mm voxels, the visual scores of 8-, 6-, and 5-mm spheres were 4.0 ± 0.00, 3.3 ± 0.50, and 1.5 ± 1.00, respectively, whereas those with 2-mm voxels were 3.8 ± 0.00, 2.5 ± 0.58, and 1.0 ± 0.00, respectively. For OSEM images with 4-mm voxels, the visual scores for 8-, 6-, and 5-mm spheres were 3.5 ± 0.58, 3.0 ± 0.82, and 1.8 ± 0.96, respectively, whereas those with 2-mm voxels were 2.8 ± 0.50, 2.0 ± 0.82, and 1.0 ± 0.00, respectively. On the other hand, for OSEM+PSF images with 4-mm voxels, the visual scores for 8-, 6-, and 5-mm spheres were 4.0 ± 0.00, 3.5 ± 0.50, and 1.5 ± 0.58, respectively, whereas those with 2-mm voxels were 4.5 ± 0.58, 3.5 ± 0.58, and 1.3 ± 0.50, respectively. The visual score for 6-mm or larger spheres with 4-mm voxels exceeded the criterion of 3. The visual score for 8-mm or larger spheres with 2-mm voxels also exceeded the criterion. Visual assessment of the 2- and 120-min acquisitions did not significantly differ among reconstruction parameters. Interobserver agreement was moderate to excellent (κ = 0.420–0.820).

Table 1 shows the CV of the background on phantom images. For OSEM+TOF and OSEM+PSF images, background noise in the NEMA phantom was lower than that for OSEM images in both the 120-min and the 2-min acquisitions, but the difference was not statistically significant. On the other hand, there was more background noise with 2-mm voxels than with 4-mm voxels in both the 120-min and the 2-min acquisitions, and this difference was statistically significant ($P < 0.05$). OSEM+PSF images showed the smallest CV on 2-min acquisitions with 2-mm voxels.

Table 2 shows DI in relation to voxel size. In 120-min acquisitions, the DI for spheres 8 mm or smaller with 2-mm voxels was higher than that with 4-mm voxels. The DI for OSEM+TOF images was higher than that for OSEM images in all spheres. OSEM+PSF images showed a higher DI for spheres 8 mm or larger than did OSEM images, but the DI for spheres smaller than 8 mm was not improved with the PSF model. Furthermore, 4-mm spheres were not detected at all on PSF images. In 2-min acquisitions, 4-mm spheres were not detected with any reconstruction algorithm. The DI for spheres 8 mm or smaller with 2-mm voxels was higher than that with 4-mm voxels. The DI for OSEM+TOF images was superior to that for OSEM images with 4-mm voxels but not with 2-mm voxels. No significant differences in the DI of spheres 8 mm or smaller was observed between 4- and 2-mm voxels with any reconstruction algorithm. OSEM+PSF images did not improve the DI for spheres smaller than 8 mm with

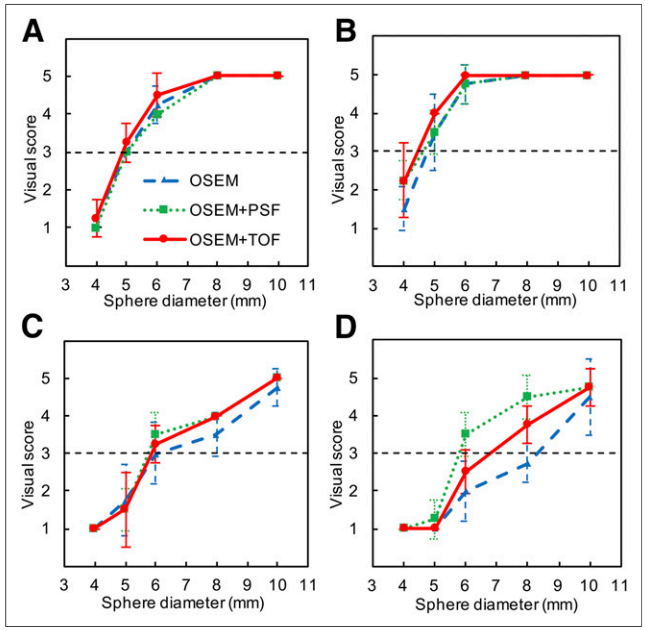

FIGURE 3. Visual assessment of PET images: 120-min (A and B) and 2-min (C and D) acquisitions; 4-mm (A and C) and 2-mm (B and D) voxel reconstructions.

TABLE 1
CV of Background on Phantom Images

Acquisition time	Voxel size	CV of background (%)*		
		OSEM	OSEM+PSF	OSEM+TOF
120 min	4 mm	2.9	2.8	2.3
	2 mm	4.4	3.7	3.5
2 min	4 mm	15.0 ± 1.4	14.0 ± 2.1	13.0 ± 1.0
	2 mm	28.7 ± 3.7	21.4 ± 3.6	24.6 ± 0.4

*Data are mean, or mean ± SD.

either 4- or 2-mm voxels. However, OSEM+PSF images showed a higher DI for spheres 8 mm or larger with both 4- and 2-mm voxels. The difference was not statistically significant.

RC in relation to voxel size is shown in Table 3. In 120-min acquisitions, the RC with 2-mm voxels was higher than that with 4-mm voxels. The RC for OSEM+TOF images was comparable to that for OSEM images with both 4- and 2-mm voxels, whereas that for OSEM+PSF images was a little lower for spheres 8 mm or smaller. In 2-min acquisitions, RC did not markedly differ between 4- and 2-mm voxels or among OSEM, OSEM+TOF, and OSEM+PSF images. The difference was not statistically significant.

DISCUSSION

In this study, we evaluated the effect of reconstruction settings on the detectability of subcentimeter hot spheres using clinical PET/CT. The TOF information improved the detectability of spheres 10 mm or smaller, in comparison to OSEM images. PSF images did not show the higher detectability for spheres 8 mm or smaller. Two-millimeter voxels improved DI and RC over 4-mm voxels.

OSEM+TOF images improved the detection of spheres 10 mm or smaller in both visual and physical assessments. Because the time resolution of the Biograph mCT PET/CT scanner was 555 ps, the probability distribution of an annihilation point was narrowed to approximately 8 cm. In clinical examinations, Fakhri et al. reported that the TOF model improved the signal-to-noise ratio for low-contrast lesions (*19*). Conti reported that TOF images allowed better detection of small lesions than non-TOF images (*20*). TOF images using 2-mm voxels were reported to improve the detection of atherosclerotic plaque inflammation with ^{18}F-FDG in small and moving phantoms (*17*). The smallest visible sphere with a sphere-to-background ratio of 8 was a 5.0-mm sphere on TOF images using 2-mm voxels but was a 6.2-mm sphere on non-TOF images. On a heavy patient (140 kg; body mass index, 46) with multiple lesions of non-Hodgkin lymphoma, the additional lesions were observed more clearly on TOF images than on non-TOF images. TOF images also lead to higher contrast and uptake (*21*). The TOF model reduced background variability, and the resulting improvement in image quality is thus considered to improve detection of subcentimeter hot spheres.

TABLE 2
Detectability in Standard- and Small-Voxel Reconstructions

Acquisition time	Voxel size	Sphere diameter (mm)*				
		4	5	6	8	10
120 min						
OSEM	4 mm	6.8	13.3	33.5	78.5	166.7
	2 mm	13.1	22.3	45.0	92.8	151.9
OSEM+PSF	4 mm	NA	11.1	30.1	77.4	195.6
	2 mm	7.1	15.8	40.9	116.1	265.4
OSEM+TOF	4 mm	9.5	19.6	48.3	105.1	211.2
	2 mm	14.6	31.3	61.2	137.2	190.3
2 min						
OSEM	4 mm	NA	3.1 ± 4.4	7.6 ± 6.2	13.6 ± 4.3	34.6 ± 11.4
	2 mm	NA	NA	12.7 ± 13.2	15.2 ± 5.6	32.2 ± 15.4
OSEM+PSF	4 mm	NA	2.8 ± 3.2	7.8 ± 6.5	14.0 ± 1.8	41.3 ± 9.4
	2 mm	NA	3.7 ± 3.0	11.4 ± 9.6	16.4 ± 2.3	47.5 ± 10.5
OSEM+TOF	4 mm	NA	4.6 ± 0.2	8.4 ± 5.1	17.0 ± 1.5	40.2 ± 10.2
	2 mm	NA	NA	12.2 ± 5.5	17.0 ± 2.5	30.3 ± 5.6

*Data are mean, or mean ± SD.
NA = not available.

TABLE 3
RC in Standard- and Small-Voxel Reconstructions

Acquisition time	Voxel size	Sphere diameter (mm)*				
		4	5	6	8	10
120 min						
OSEM	4 mm	0.12	0.13	0.19	0.32	0.56
	2 mm	0.14	0.17	0.26	0.45	0.68
OSEM+PSF	4 mm	NA	0.12	0.16	0.28	0.58
	2 mm	0.11	0.13	0.21	0.44	0.90
OSEM+TOF	4 mm	0.12	0.14	0.20	0.33	0.56
	2 mm	0.13	0.18	0.27	0.50	0.67
2 min						
OSEM	4 mm	NA	0.12 ± 0.05	0.18 ± 0.08	0.25 ± 0.06	0.52 ± 0.17
	2 mm	NA	NA	0.22 ± 0.18	0.26 ± 0.11	0.53 ± 0.29
OSEM+PSF	4 mm	NA	0.11 ± 0.03	0.16 ± 0.06	0.24 ± 0.04	0.56 ± 0.15
	2 mm	NA	0.12 ± 0.04	0.22 ± 0.11	0.32 ± 0.10	0.80 ± 0.30
OSEM+TOF	4 mm	NA	0.14 ± 0.01	0.18 ± 0.05	0.27 ± 0.02	0.53 ± 0.07
	2 mm	NA	NA	0.22 ± 0.09	0.27 ± 0.01	0.45 ± 0.03

*Data are mean, or mean ± SD.
NA = not available.

The PSF model did not successfully improve detection of spheres 8 mm or smaller. Kidera et al. reported that the PSF model resulted in the greatest increase in contrast RC for 13-mm hot spheres. Spheres between 10 and 17 mm showed improvement in contrast RC, whereas no such improvement was noted for larger spheres (*22*). Our results also showed that PSF correction increased the DI in spheres 8 mm or larger but not in spheres smaller than 8 mm. This finding suggests that the effect of the PSF model is dependent on sphere size. However, the PSF model did improve the visual score for the 2-min acquisition more than OSEM alone. Akamatsu et al. reported that the PSF model had a smoothing effect on PET images (*7*). In a clinical study, the PSF model improved the sensitivity of PET in detecting axillary node involvement, especially for patients in whom the largest nodal metastasis was smaller than 7 mm (*18*). In our study, the CV of the background on PSF images was lower than that on OSEM images. The reduced background variability with the PSF model is considered to have contributed to this improvement.

Two-millimeter voxels improved the detection of spheres 8 mm or larger in both visual and physical assessments for 120-min acquisitions. Koopman et al. reported that 2-mm voxels significantly improved the signal-to-noise ratio and RC for 5- to 8-mm spheres (*23*). Adler et al. reported a high detection score for visual assessment with 2-mm voxels, compared with 4-mm voxels (*24*). Two-millimeter voxels improve spatial resolution and reduce the partial-volume effect. A sufficient acquisition time reduces background variability and improves DI. In high-count statistics, 2-mm voxels improved DI. In contrast, 2-mm voxels did not successfully improve the detection of small spheres for 2-min acquisitions. The short acquisition increases background variability. The smoothing effect of the PSF model is considered to improve detectability in low-count statistics.

Several limitations of the present study warrant mention. First, we used only a single phantom simulating a patient with small lesions. Further examinations with more varied patients such as those with lymph node metastasis and arteriosclerosis should be performed. Second, we did not determine what acquisition time would be adequate for small-lesion detection. A 120-min acquisition is unrealistic for a patient examination, whereas a 2-min acquisition may not be sufficient. It is necessary to determine the acquisition time adequate for each institution and device. Third, the only sphere-to-background ratio that we examined was 8. The edge artifacts due to the PSF model are considered to vary with sphere-to-background ratio (*9*). Therefore, other sphere-to-background ratios should be examined. Forth, the influence of a smoothing filter on small-lesion detection was not evaluated in this study. The outcome of the PSF model with PET images of subcentimeter lesions depends on optimization of the smoothing filter (*25*). We should therefore determine the ideal smoothing filter.

CONCLUSION

The TOF model with 2-mm voxels was proved to improve the detectability of spheres 10 mm or smaller using a clinical PET/CT scanner at our institution. In contrast, the PSF model did not successfully improve detectability or RCs for spheres 8 mm or smaller. The ideal reconstruction parameters should be determined for each institution.

DISCLOSURE

No potential conflict of interest relevant to this article was reported.

ACKNOWLEDGMENT

We thank the staff of the Department of Clinical Radiology and Medical Technology at Kyushu University Hospital for their valuable clinical support.

REFERENCES

1. Sahiner I, Vural GU. Positron emission tomography/computerized tomography in lung cancer. *Quant Imaging Med Surg.* 2014;4:195–206.
2. Poeppel TD, Krause BJ, Heusner TA, et al. PET/CT for staging and follow-up of patients with malignancies. *Eur J Radiol.* 2009;70:382–392.
3. Ben-Haim S, Ell P. ^{18}F-FDG PET and PET/CT in the evaluation of cancer treatment response. *J Nucl Med.* 2009;50:88–99.
4. Soret M, Bacharach SL, Buvat I. Partial-volume effect in PET tumor imaging. *J Nucl Med.* 2007;48:932–945.
5. Sunderland JJ, Christian PE. Quantitative PET/CT scanner performance characterization based upon the Society of Nuclear Medicine and Molecular Imaging Clinical Trials Network oncology clinical simulator phantom. *J Nucl Med.* 2015; 56:145–152.
6. Fukukita H, Suzuki K, Matsumoto K, et al. Japanese guideline for the oncology FDG-PET/CT data acquisition protocol: synopsis of version 2.0. *Ann Nucl Med.* 2014;28:693–705.
7. Akamatsu G, Ishikawa K, Mitsumoto K, et al. Improvement in PET/CT image quality with a combination of point-spread function and time-of-flight in relation to reconstruction parameters. *J Nucl Med.* 2012;53:1716–1722.
8. Moses WW. Recent advances and future advances in time-of-flight PET. *Nucl Instrum Methods Phys Res A.* 2007;580:919–924.
9. Lois C, Jakoby BW, Long MJ, et al. An assessment of the impact of incorporating time-of-flight information into clinical PET/CT imaging. *J Nucl Med.* 2010; 51:237–245.
10. Rahmim A, Qi J, Sossi V. Resolution modeling in PET imaging: theory, practice, benefits, and pitfalls. *Med Phys.* 2013;40:064301.
11. Tong S, Alession AM, Kinahan PE. Noise and signal properties in PSF-based fully 3D PET image reconstruction: an experimental evaluation. *Phys Med Biol.* 2010;55:1453–1473.
12. Panin VY, Kehren F, Michel C, et al. Fully 3-D PET reconstruction with system matrix derived from point source measurements. *IEEE Trans Med Imaging.* 2006;25:907–921.
13. Varrone A, Sjöholm N, Eriksson L, et al. Advancement in PET quantification using 3D-OP-OSEM point spread function reconstruction with the HRRT. *Eur J Nucl Med Mol Imaging.* 2009;36:1639–1650.
14. Taniguchi T, Akamatsu G, Kasahara Y, et al. Improvement in PET/CT image quality in overweight patients with PSF and TOF. *Ann Nucl Med.* 2015;29:71–77.
15. Jakoby BW, Bercier Y, Watson CC, et al. Performance characteristics of a new LSO PET/CT scanner with extended axial field-of-view and PSF reconstruction. *IEEE Trans Nucl Sci.* 2009;56:633–639.
16. Kadrmas DJ, Casey ME, Conti M, et al. Impact of time-of-flight on PET tumor detection. *J Nucl Med.* 2009;50:1315–1323.
17. Suda M, Kiriyama T, Ishihara K, et al. The high matrix acquisition technique for imaging of atherosclerotic plaque inflammation in fluorine-18 fluorodeoxyglucose positron emission tomography/computed tomography with time-of-flight: phantom study. *J Nucl Cardiol.* 2017;24:1161–1170.
18. Bellevre D, Blanc Fournier C, Switsers O, et al. Staging the axilla in breast cancer patients with ^{18}F-FDG PET: how small are the metastases that we can detect with new generation clinical PET systems? *Eur J Nucl Med Mol Imaging.* 2014;41:1103–1112.
19. El Fakhri G, Surti S, Trott CM, et al. Improvement in lesion detection with whole-body oncologic time-of-flight PET. *J Nucl Med.* 2011;52:347–353.
20. Conti M. Focus on time-of-flight PET: the benefits of improved time resolution. *Eur J Nucl Med Mol Imaging.* 2011;38:1147–1157.
21. Karp JS, Surti S, Daube-Witherspoon ME, et al. Benefit of time-of-flight in PET: experimental and clinical results. *J Nucl Med.* 2008;49:462–470.
22. Kidera D, Kihara K, Akamatsu G, et al. The edge artifact in the point-spread function-based PET reconstruction at different sphere-to-background ratios of radioactivity. *Ann Nucl Med.* 2016;30:97–103.
23. Koopman D, van Dalen JA, Lagerweij MC, et al. Improving the detection of small lesions using a state-of-the-art time-of-flight PET/CT system and small-voxel reconstructions. *J Nucl Med Technol.* 2015;43:21–27.
24. Adler S, Seidel J, Choyke P, et al. Minimum lesion detectability as a measure of PET system performance. *EJNMMI Phys.* 2017;4:13.
25. Munk OL, Tolbod LP, Hansen SB, et al. Point-spread function reconstructed PET images of sub-centimeter lesions are not quantitative. *EJNMMI Phys.* 2017;4:5.